Research Article | Vol. 29, No. 22 / 25 Oct 2021 / Optics Express 36546
Optics EXPRESS

Thermal noise computation of arbitrary masses in optical interferometers from first principles

JOHANNES DICKMANN*

Technische Universität Braunschweig, Laboratory for Emerging Nanometrology LENA, Langer Kamp 6a/b, D- 38106 Braunschweig, Germany
j.dickmann@tu-bs.de

Abstract: Thermal noise of optical components is one of the sensitivity limiting effects in gravitational wave detectors, laser stabilization cavities and many other experiments in basic research. However, current methods for the computation of thermal noise are limited for an application in either infinitely large or symmetrically illuminated masses. I present a general method of computing thermal noise of arbitrary finite-sized masses in optical interferometers. The presented approach generalizes state-of-the-art methods for an application in arbitrary shaped optical elements illuminated by arbitrary spatial light distributions. Furthermore, I show the application of the presented approach to compute thermal noise of maladjusted mirrors in Fabry-Perot interferometers. It is shown that the noise can be reduced by off-axis illumination in the case of thin mirrors.

1. Introduction

Thermal fluctuations are one of the most dominant noise sources for many interferometric applications like gravitational wave detectors [1] and laser stabilization cavities [2] used for various applications like atom interferometry [3], geodesy [4] and the search for dark matter [5,6]. Thus, thermal noise limits the stability and accuracy of such systems [2]. In general, thermal noise of interferometric components is calculated using the fluctuation-dissipation theorem (FDT) approach by Levin [7]. A generalization of this method for arbitrary shaped surfaces is based on the Maxwell stress tensor [8]. The purpose of this paper is to generalize the two formalisms for a broader use in more complex optical systems, for example asymmetrically illuminated cavities.

In section 2, the novel formalism is presented. In section 3, the validity of the new method for a well-known system — the end mirror of a Michelson interferometer — compared to previous methods is proven. In the last section 4, the formalism is applied to compute the effect of a maladjusted mirror in a Fabry-Perot cavity as laser stabilization optical resonator. As we will discuss later, the formalism is meta-stable. That means, the investigation of a stabilizing method for the numerical computation is mandatory. This method is briefly explained in the Appendix A. In Appendix B, the presented method is compared to straight-forward rigid motion suppression using fixed constraints.

A brief outline of the method follows: The fluctuation-dissipation theorem approach by Levin [7] is based on a virtual oscillating pressure. This pressure is obtained by applying the Maxwell stress tensor $\hat{\sigma}$ over the entire surface of the optical device under investigation [8]. In other words, the virtual pressure must be weighted with the intensity distribution in order to follow the optical readout. The total virtual force F_0 is equal to the surface integral of the ponderomotive pressure. This pressure induces a storage of elastic deformation power inside the optical device W_{def}. Farther, the pressure leads to a mechanical motion of the whole optical device in general. This accelerating motion leads to an error in the computation of W_{def} induced by the moments of inertia. To obtain the correct elastic power, a formalism of compensating the moments of inertia is presented. The presence of an intrinsic mechanical loss of the optical device Φ [9] leads to a dissipation of elastic power. The temporal average of this power is called W_{diss} hereinafter. So,

#438507 https://doi.org/10.1364/OE.438507
Journal © 2021 Received 21 Jul 2021; revised 18 Sep 2021; accepted 20 Sep 2021; published 21 Oct 2021

Optics EXPRESS

the spectral density of fluctuations of the read-out length can be written as [7]:

$$S(f) = \frac{2k_B T}{\pi^2 f^2} \frac{W_{\text{diss}}}{F_0^2}, \tag{1}$$

where k_B and T are the Boltzmann's constant and the temperature of the optical device, respectively. f represents the mechanical read-out frequency. The dissipated power can be calculated as follows:

$$W_{\text{diss}} = 2\pi f \iiint_V \Phi(\vec{r}) e_{\text{elast}}(\vec{r}) d^3 r, \tag{2}$$

where e_{elast} denotes the elastic energy density stored inside the optical system during one period of oscillation. The integration is performed over the volume V of the optical device.

2. Moments of inertia compensation

The pressures applied to the surfaces of the optical device lead to an accelerated motion of itself. To apply the fluctuation-dissipation theorem, two conditions must be fulfilled [10]: First, the optical device is in elastic equilibrium. That means, the internal stresses are in equilibrium with the external force. Second, the optical device does not accelerate. More precisely, the velocity of the center of mass and the rotation state of the optical device are both stationary. To fulfill the first requirement, the elastic energy is evaluated in the limit of an infinite time [11]. The application of a tailored force field $\vec{f}(\vec{r})$ ensures the fulfillment of the second requirement. The force field appears as a volume force density $\vec{f}$ with resulting net force $\vec{F}$ and net torque $\vec{M}$:

$$\begin{aligned} \vec{F} &= \iiint_V \vec{f} d^3 r, \\ \vec{M} &= \iiint_V \vec{r} \times \vec{f} d^3 r, \end{aligned} \tag{3}$$

where V indicates the volume of the optical device. Please note that the formalism is valid for arbitrary volume-mass density distributions.

The following scheme leads to a tailored force field, which compensates all parts of the elastic energy due to the moments of inertia. The calculations are performed for a static optical device, so that the pressures applied to the surfaces are constant. This is allowed, because after applying the force field, the optical device is indeed in spatial equilibrium. The compensating force volume density consists of two parts: The first part, $\vec{f}_{\text{trans}}$, compensates the acceleration of the center of mass. The second part, $\vec{f}_{\text{rot}}$, compensates the accelerated rotation due to the net torque:

$$\vec{f} = \vec{f}_{\text{trans}} + \vec{f}_{\text{rot}}. \tag{4}$$

The first part can be compensated by means of a constant volume force density

$$\vec{f}_{\text{trans}} = -\frac{1}{V} \iint_{\partial V} \Delta\hat{\sigma} \cdot d\vec{A}, \tag{5}$$

where $\vec{A}$ is the surface area pointing along the area's normal vector and V is the volume of the optical device, respectively. $\Delta\hat{\sigma}(\vec{r})$ represents the ponderomotive pressure due to Maxwell's stress [8]. It is defined as the difference between the stress tensors inside and outside the material

Optics EXPRESS

of the optical device directly at the surface. For Cartesian coordinates and SI units, it reads:

$$\Delta\hat{\sigma}(\vec{r}) = \lim_{\vec{r}\uparrow\partial V} \hat{\sigma} - \lim_{\vec{r}\downarrow\partial V} \hat{\sigma}, \tag{6}$$

$$\sigma_{ij} = \epsilon_0\epsilon_r E_i E_j + \frac{1}{\mu_0\mu_r} B_i B_j - \frac{1}{2}\left(\epsilon_0\epsilon_r E^2 + \frac{1}{\mu_0\mu_r} B^2\right)\delta_{ij}, \tag{7}$$

where E_i and B_i ($i \in \{x, y, z\}$) represent the components of the electric field and magnetic flux density, respectively. δ_{ij} is the Kronecker's symbol. To determine the second part of the accelerating motion, the net rotation, we apply the first volume force $\vec{f}_{\text{trans}}$, so that the center of mass of the optical device is static. Now we are able to compute the rotation axis and the net torque under the influence of the light pressures. Without loss of generality, we define the readout direction with the normalized vector $\vec{r}_{\text{read}}$, and the direction of the rotation axis $\vec{r}_{\text{rot}}$ being parallel to the net torque (compare Fig. 1). The torque due to ponderomotive pressures is equal to:

$$\vec{M} = \iint_{\partial V} \vec{r} \times \left(\Delta\hat{\sigma} \cdot d\vec{A}\right). \tag{8}$$

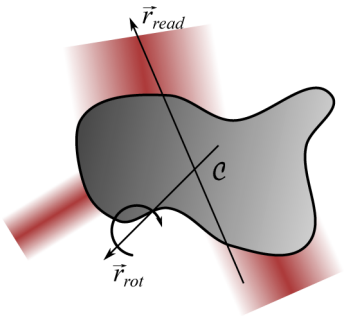

Fig. 1. Sketch of a cross-section of the optical device (here in gray color). The rotation axis is parallel to $\vec{r}_{\text{rot}}$ and intersects the point of origin, which is the center of mass C. The light pressures are indicated by the red colored beams. $\vec{r}_{\text{read}}$ indicates the readout direction.

The rotation axis intersects the center of mass, which is at the origin of the coordinate system. To compensate the constant torque $\vec{M}$, a linear volume force density is introduced:

$$\vec{f}_{\text{rot}} = -\frac{1}{V}\hat{\gamma} \cdot \vec{r}, \tag{9}$$

where $\hat{\gamma}$ represents a constant tensor of order 2 in the three dimensions x, y, z of the coordinate system bound to the optical device. However, to compute the components of $\hat{\gamma}$, the light field at the surface of the optical device and thus Maxwell's stress tensor $\hat{\sigma}(\vec{r})$ must be known. The components of $\hat{\gamma}$ result from the required torque compensation:

$$\iint_{\partial V} \vec{r} \times \left(\Delta\hat{\sigma} \cdot d\vec{A}\right) = \frac{1}{V}\iiint_{V} \vec{r} \times (\hat{\gamma} \cdot \vec{r}) d^3 r. \tag{10}$$

3. Proof of validity: mirror thermal noise of Michelson interferometers

In this section, I will show that the presented formalism leads to the same result as state-of-the-art formalism for a well-known system. Thus, we have to choose a model system that can be handled by the state-of-the-art application of fluctuation-dissipation theorem. The probably most popular

Optics EXPRESS

system in this sense is a test mass of a gravitational wave detector as the end mirror of a Michelson interferometer [7]. This mirror is finite-sized and it is illuminated perfectly symmetrically by a Gaussian shaped beam (compare Fig. 2):

$$\begin{aligned} I(\vec{r}) &= \frac{I_0}{\pi r_0^2} \exp\left(-\frac{r^2}{r_0^2}\right) \\ \iint_{\partial V} I(\vec{r}) dA &= I_0 \left(1 - \exp\left(-\frac{R^2}{r_0^2}\right)\right), \end{aligned} \tag{11}$$

where r_0 represents the Gaussian beam radius, r is the distance on the illuminated mirror surface measured from its center (compare Fig. 2) and R the radius of the mirror itself, respectively. The readout direction is parallel to z. In order to apply the fluctuation dissipation theorem we have to weigh the virtual pressure with the readout intensity distribution. Thus, we can utilize the Maxwell stress tensor for a perfectly reflecting mirror:

$$\Delta\sigma_{ij} = \begin{cases} -2\frac{I(\vec{r})}{c} & , \quad \text{for } i,j = z \\ 0 & , \quad \text{else} \end{cases}, \tag{12}$$

where c represents the vacuum light speed.

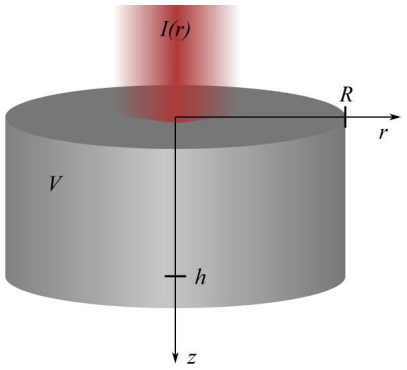

Fig. 2. Sketch of the end mirror under investigation. The readout light intensity $I(r)$ is visualized in red color. The mirror volume V is defined by the mirror radius R and mirror height h. The cylindrical coordinate system is chosen with respect to the mirror geometry.

In order to proceed with the procedure presented in section 2 the translation force field is computed:

$$\vec{f}_{\text{trans}} = \frac{1}{V} \iint_{\partial V} 2\frac{I(\vec{r})}{c} dA \vec{e}_z = \frac{2I_0}{Vc} \left(1 - \exp\left(-\frac{R^2}{r_0^2}\right)\right) \vec{e}_z. \tag{13}$$

The net torque acting on the mirror is zero:

$$\vec{M} = -\frac{2}{c} \iint_{\partial V} \vec{r} \times \left(I(\vec{r}) \vec{e}_z dA\right) = 0. \tag{14}$$

Obviously, the torque compensating force field is zero as well:

$$\hat{\gamma} = \hat{0}. \tag{15}$$

The elastic energy is computed using the finite elements tool COMSOL [12]. Using the fluctuation dissipation theorem, Eq. (1), thermal noise power spectral density can be evaluated

Optics EXPRESS

for the mirror. We compare the results with those from Bondu, Hello & Vinet [13], corrected by Liu & Thorne [14]. This comparison is shown in Fig. 3 for the parameters listed in tab. 1. The results by Bondu, Hello & Vinet [13] were obtained by ignoring the linear force, i.e. by not compensating the mirror's moment of inertia. Liu & Thorne [14] corrected these results by including the inertia compensation. These corrected values are in perfect agreement with the results obtained with the presented method.

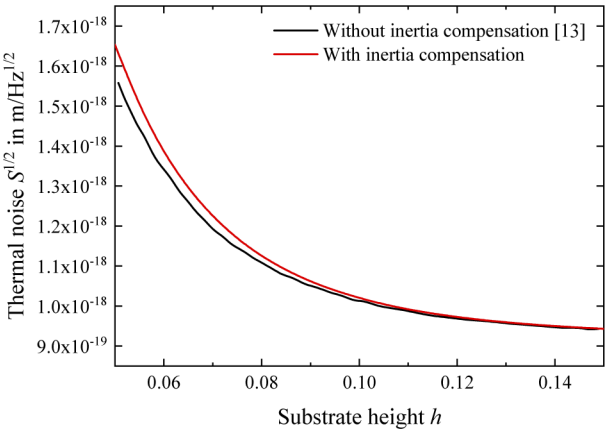

Fig. 3. Thermal noise spectral amplitude of one end-mirror of a Michelson interferometer at a frequency of 1 Hz and a temperature of 293 K. The results of the here presented formalism are highlighted in red color. The black curve shows the results by Bondu, Hello & Vinet [13] without compensation of inertia. The corrected values by Liu & Thorne [14] are in perfect agreement with the red curve (no deviations apparent). For more parameters, see Table 1.

Table 1. Design parameters of the mirror of the Michelson interferometer under investigation.

Parameter	Value
Young's modulus Y	73 GPa
Poisson's ratio ν	0.166
Gaussian beam radius r_0	$2\sqrt{2}$ cm
Mirror radius R	17.5 cm
Mechanical loss Φ	10^{-6}

4. Effect of a maladjusted mirror

After confirming the consistency of the presented approach, we can proceed with a non-symmetrical system. The system of choice is the sub-40-mHz-linewidth laser based on a silicon single-crystal optical cavity [2], Fig. 4. This system consists of a Fabry-Perot-Cavity with two mirrors. The geometrical parameters are shown in tab. 2.

In the following two sections, the optical and thermal noise performance are analyzed for a maladjusted mirror (i.e. beam displacement a).

Optics EXPRESS

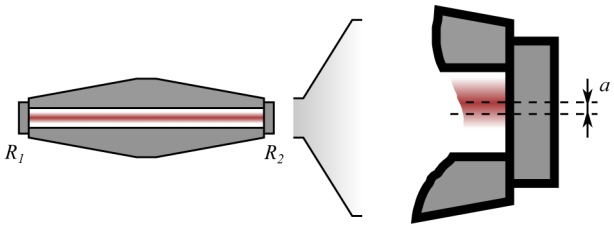

Fig. 4. Sketch of a cross-section of the optical cavity. a determines the displacement of the beam to the symmetrical axis of the cavity.

Table 2. Design parameters of the optical Fabry-Perot interferometer under investigation. [2]

Parameter	Value
Cavity length L	210 mm
Central bore diameter $2R$	5 mm
Gaussian beam radius r_0	483 μm
Laser wavelength λ	1.5 μm
Mirror diameter D	12.7 mm
Mirror thickness h	5 mm

4.1. Optical performance

The light field inside the cavity is assumed to have a spatial Gaussian shape. Thus, the spatial intensity distribution reads:

$$I(\vec{r}) = \frac{I_0}{\pi r_0^2} \exp\left(-\frac{r^2}{r_0^2}\right), \qquad \iint_{\partial V} I(\vec{r}) dA = P_0, \tag{16}$$

where r represents the distance from the center of the beam. In a first step, the effect of the displacement a on the maximum cavity finesse is investigated. The influence of non-perfect mirrors is neglected (e.g. scattering, absorption). We study the effect of the finite mirror surface, limited by the bore radius of the cavity. The finesse of the cavity is given by the reflectivity of the two mirrors, R_1 and R_2 [15]:

$$\mathcal{F} \approx \frac{\pi \sqrt[4]{R_1 R_2}}{1 - \sqrt{R_1 R_2}}. \tag{17}$$

In this analysis, one mirror is perfectly centered with respect to the laser beam. Without loss of generality, the maximum reflectivity R_1 of this mirror reads:

$$R_1 = \frac{1}{I_0} \iint_{\text{bore}} I(\vec{r}) dA = 1 - \exp\left(-\frac{R^2}{r_0^2}\right) \to 1. \tag{18}$$

The second reflectivity is computed equally. The beam is shifted by a radially with respect to the symmetry axis of the cavity:

$$I(\vec{r}) = \frac{I_0}{\pi r_0^2} \exp\left(-\frac{x^2 + (y-a)^2}{r_0^2}\right). \tag{19}$$

Optics EXPRESS

Thus, the second maximum reflectivity reads:

$$R_2 = 1 - \exp\left(-\frac{R^2 + a^2}{r_0^2}\right)\mathcal{I}_0\left(\frac{2aR}{r_0^2}\right) + \frac{a}{2\sqrt{\pi}r_0}\int_0^{2\pi} \sin\varphi \exp\left(-\frac{a^2\cos^2\varphi}{r_0^2}\right)\mathrm{erf}\left(\frac{R - a\sin\varphi}{r_0}\right)d\varphi, \tag{20}$$

where $\mathcal{I}_0$ represents the modified Bessel function of first kind:

$$\mathcal{I}_0(x) = \sum_{m=0}^{\infty}\frac{1}{(m!)^2}\left(\frac{x}{2}\right)^{2m}, \tag{21}$$

and erf(x) represents the error function:

$$\mathrm{erf}(x) = \frac{2}{\sqrt{\pi}}\int_0^x e^{-t^2}dt. \tag{22}$$

The integral in Eq. (20) is computed numerically. The maximum finesse of the cavity is shown in Fig. 5 with respect to the relative beam displacement a/R for different ratios of the beam radius and the bore radius r_0/R.

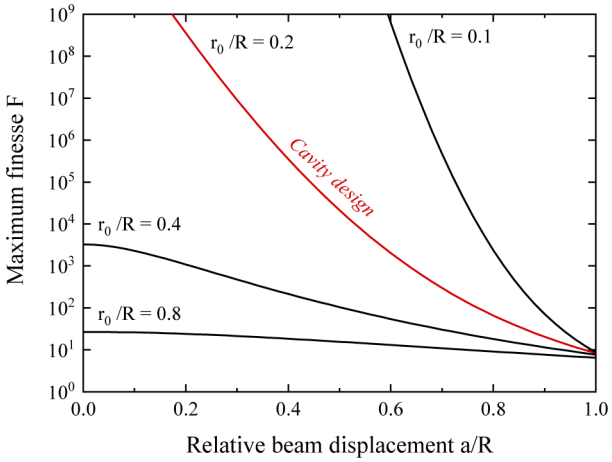

Fig. 5. Maximum finesse of the cavity versus relative beam displacement on one mirror for different ratios r_0/R. The cavity design used in this article is marked in red.

4.2. Thermal noise performance

The Brownian displacement noise is calculated using the formalism introduced in section 2. The readout direction is pointing to z (without loss of generality). For the claimed total reflectivity of the mirror, the ponderomotive pressure is equal to Eq. (12). Thus, the translation compensating force density field reads

$$\vec{f}_{\mathrm{trans}} = \frac{1}{V}\iint_{\mathrm{bore}} 2\frac{I(\vec{r})}{c}dA\vec{e}_z = \frac{2}{Vc}I_0R_2\vec{e}_z, \tag{23}$$

utilizing the reflectivity R_2 computed in the previous section, Eq. (20). The results for the translation part of the compensation force density field are shown in Fig. 6 (left). The net torque

Optics EXPRESS

due to the light pressure reads

$$\vec{M} = -\frac{2}{c}\iint_{\text{bore}} yI(\vec{r})dA\vec{e}_x = -\frac{2I_0}{\pi c r_0^2}\int_0^{2\pi}\int_0^R r^2 \sin\varphi \exp\left(-\frac{r^2 - 2ar\sin\varphi + a^2}{r_0^2}\right) dr d\varphi. \tag{24}$$

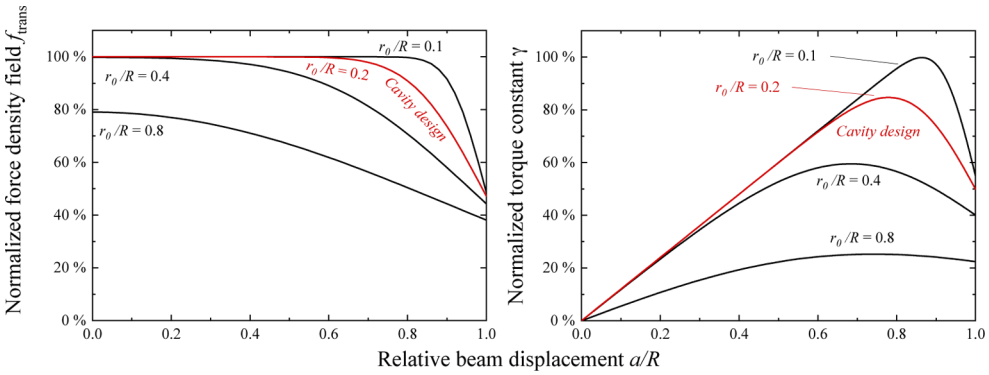

Fig. 6. Left: Normalized force density field for the compensation of translation motions versus relative beam displacement a/R for different ratios r_0/R. Right: Numerically computed and normalized constant γ for the compensation of torque versus relative beam displacement a/R for different ratios r_0/R.

Thus, the torque compensation force density field contains only a y-component in z direction. In this sense, the tensor $\hat{\gamma}$ simplifies in the following way:

$$\hat{\gamma} = \begin{pmatrix} 0 & 0 & 0 \\ 0 & 0 & 0 \\ 0 & \gamma & 0 \end{pmatrix}. \tag{25}$$

Using Eq. (10), we are able to compute the constant γ. This computation was performed numerically. The results can be seen in Fig. 6. For the case $r_0, a \ll R$, it simplifies in the following way:

$$\gamma \longrightarrow \frac{8I_0 a}{R^2 c}. \tag{26}$$

Now we are able to compute the elastic energies, introduced in sec. 1. This evaluation is performed using the finite elements tool COMSOL [12]. As simulation parameters, the optical cavity design (see Fig. 4 and tab. 2) was used. The simulation was carried out for different substrate heights h between $5r_0$ and $20r_0$ and different beam displacements a ranging from 0 to R, respectively. The results are shown in Fig. 7. Please note that the graph shows relative changes. A comparison to the noise results obtained by straight-forward rigid motion suppression in the finite element solver is discussed in Appendix B.

Even though the noise of thin substrates is higher than for more massive ones, it shows a minimum for that case. An intuitive explanation for the minimum is the fact, that the fundamental mechanical mode dominates the thermal noise at low frequencies as considered in this article. The mode shape is illustrated as inset in Fig. 8. For increasing beam displacement, the motion of this mode is read out less severely. However, for very large beam displacements, the virtual force F_0 decreases and thus the noise increases drastically, compare Eq. (1). The strength of this minimum disappears for the case of thick substrates $h \gg r_0$ and transforms to a plateau of

Optics EXPRESS

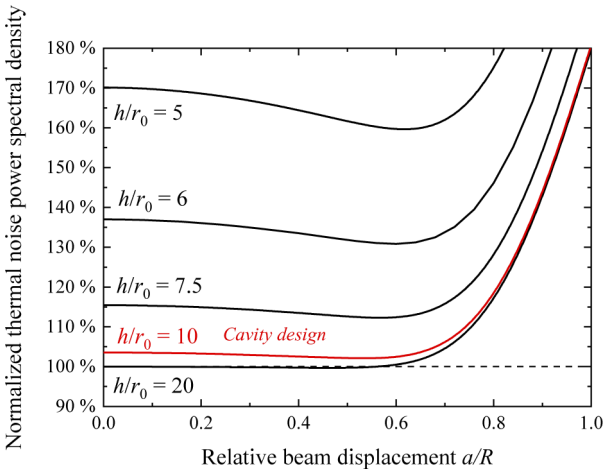

Fig. 7. Normalized thermal noise power spectral density versus beam displacement for a Fabry-Perot cavity mirror for different ratios of substrate height to beam radius h/r_0. The cavity design is highlighted in red color.

constant (low) noise level. This noise level is well-known from [13] for the case of large mirrors $h, R \gg r_0$:

$$S_{\text{plateau}} = \frac{4k_B T}{(2\pi)^{3/2} f} \frac{1-\nu^2}{r_0 Y} \Phi, \tag{27}$$

where ν is the Poisson's ratio and Y is the Young's modulus of the material. The beam position leading to minimized thermal noise depends on the ratio of mirror height to Gaussian beam radius. This dependency is also evaluated numerically and shown in Fig. 8 (black line). For larger mirror heights h/r_0, the optimized beam position for minimum noise decreases. However, in the case of thin mirrors $h<r_0$, the optimized displacement approaches a value of $a \approx 0.7R$. The resulting thermal noise at this optimized offset position was evaluated. The results are depicted in Fig. 8 (red line). It turns out, that the thermal noise and the relative mirror height h/r_0 are

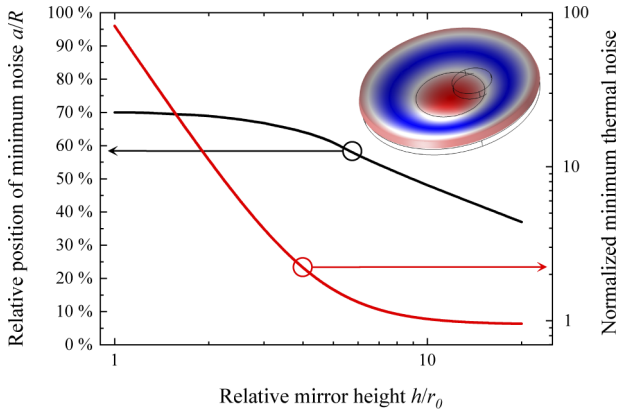

Fig. 8. Left vertical axis (black line): Relative beam positions a/R for minimum thermal noise versus relative mirror height h/r_0. Right vertical axis (red line): Normalized thermal noise power spectral density at the minimum position versus relative mirror height h/r_0. Inset: Illustration of the mirror fundamental mode and off-centered readout position.

Optics EXPRESS

connected by a power law with a coefficient of determination (r^2) >0.99999. Thus, the minimum thermal noise of the thin mirror normalized to the plateau value of infinitely large mirrors can be written as:

$$\frac{S(h/r_0)}{S_{\text{plateau}}} = 1 + C\left(\frac{h}{r_0}\right)^{-3}, \tag{28}$$

where C is a constant depending on the mirror radius R.

5. Conclusion

In this article, a general method for the computation of thermal noise of arbitrary finite-sized masses in optical interferometers is presented. This approach delivers consistent results compared to previous methods for symmetrical optical devices under symmetrical illumination. It generalizes state-of-the-art methods towards an application for arbitrary shaped optical devices under any desired illumination. The method is based on an equation for the determination of a torque-compensating tensor $\hat{\gamma}$, Eq. (10), whereby the thermal noise can be calculated efficiently. The formalism was applied to evaluate thermal noise of maladjusted interferometer mirrors. It turned out, that the thermal noise does not rise drastically as long as the displacement of the beam is smaller than 50% of the mirror radius. Indeed, a small decrease of the noise power spectral density of about 1.5% under realistic conditions can be predicted for optimized off-axis illumination. It was found, that the thermal noise of thin mirrors decreases for the case of off-axis illumination. For this case of optimized asymmetrical illumination, a power law describing the correlation between optimized thermal noise and effective mirror thickness was discovered. The presented general approach will streamline the optimization and the design of future interferometers at the frontiers of metrology.

A. Appendix: Stability of the numerical analysis

As stated in sec. 2, the spatial state of the optical device is meta-stable. In other words, for infinitely small deviations in the compensating force density field $\vec{f}$, the net force or torque are not equal to zero. This leads to an accelerated motion of the optical device (compare Fig. 9) (left).

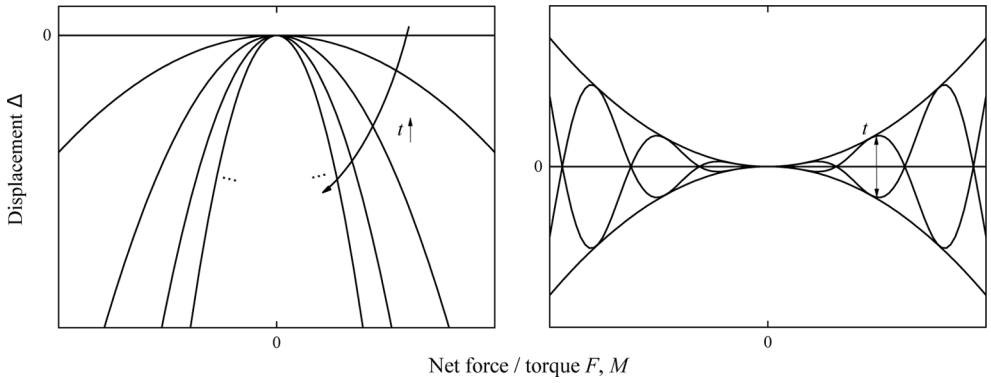

Fig. 9. Qualitative picture of the instability of the compensation method for two following cases: Left: Static case. For small changes in the net force or torque, the optical system moves on and on and does not converge to the spatially static case for the evaluation of the strain energy. Right: The dynamic case of low frequencies. The optical system moves harmonically around the static position.

A possible solution to avoid this instability is the crossover from a static analysis towards a computation at low frequencies. By means of energy, the accelerating motion of the optical

Optics EXPRESS

device arises as a constant offset. To avoid this offset, the whole system (the ponderomotive pressures and the compensating force density field) is modulated with a low frequency ξ:

$$\begin{aligned} \Delta\hat{\sigma}' &= \Delta\hat{\sigma} \times \sin(\xi t), \\ \vec{f}' &= \vec{f} \times \sin(\xi t). \end{aligned} \tag{A1}$$

The frequency must be much smaller than the lowest resonant frequency of the optical device in this case. By using this technique, the stability plot Fig. 9 (left) changes to Fig. 9 (right). Exactly this technique was used to determine the energies in sections 3 and 4.

The higher the utilized frequency ξ, the smaller is the effective displacement Δ, but the larger is the error due to resonant effects in the solid. Thus, a trade-off between the displacement accuracy and the resonant errors must be found. To show this process exemplary, the analysis of sec. 3 for a mirror with parameters listed in tab. 1 and a mirror thickness of 5 cm is used.

In Fig. 10, the evaluated elastic energy is plotted as function of the frequency ξ. We obtain the typical frequency response of a harmonic oscillator: The response function is equal to 1 for low frequencies, in the resonant case it is larger than 1 and then it decays rapidly. In the graph, there are other features, which can be identified as eigenmodes of the mirror. For the computations in sections 3 and 4, a simulation frequency of $\xi = 2.5$ Hz was used, which causes an energy error of

$$\Delta E_{\text{elast}}/E_{\text{elast}} < 10^{-6}. \tag{A2}$$

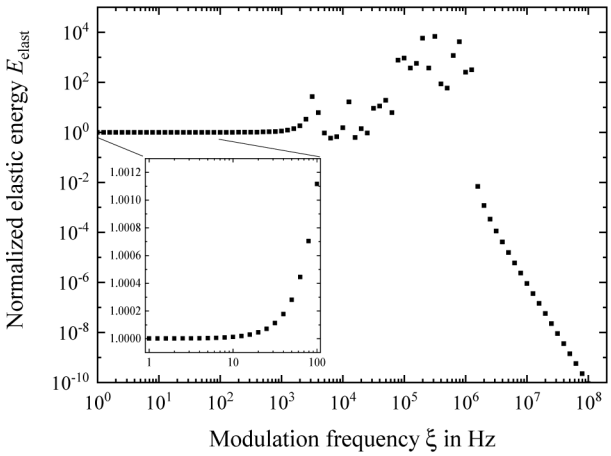

Fig. 10. Normalized elastic energy, evaluated from COMSOL simulations versus modulation frequency ξ. The inset shows the flat energy behavior in the frequency range between 1 and 100 Hz.

Please note, that the simulation frequency ξ is not connected to the readout frequency f (compare Eq. (1), fluctuation dissipation theorem). The simulation frequency ξ is a purely virtual parameter to ensure a converging finite element computation, whereas the readout frequency f influences the thermal noise.

B. Comparison to rigid motion suppression

A straight-forward option for the suppression of optical system (i.e. mirror) motion is the use of fixed constraints in the COMSOL simulation. For very large mirrors compared to the optical readout (i.e. beam diameter), this option provides accurate results, if the fixed surfaces are well-chosen. Each surface being far away from the readout beam is well suited, because the

Optics EXPRESS

motion of these surfaces is negligible. In contrast, it is not possible to find suitable surfaces in the case of small optical systems compared to the optical readout. For the cavity design investigated in this publication, the best suited surface for the application of fixed constraints is the outer wall of the cylindrical mirror. Figure 11 shows the results in terms of normalized thermal noise power spectral density obtained by applying the two different methods: The black line corresponds to the computation with fixed constraints, the red line is obtained by the approach presented in this article. The fixed constraint computation delivers about 3 % overestimated thermal noise originated by additional stresses close to the fixed surface. However, the crucial discrepancy can be seen for the case of off-axis illumination. The fixed constraint computation shows a monotonically increasing noise for increasing beam displacement a, whereas the compensating force field method manifests in a minimum noise at a certain beam displacement.

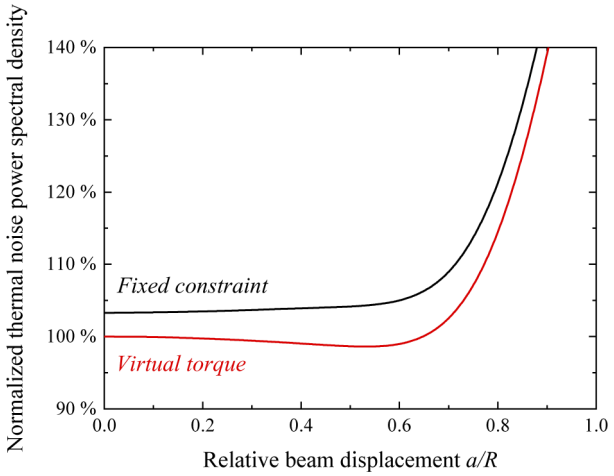

Fig. 11. Normalized thermal noise power spectral density versus relative beam displacement a/R. The black line results from the COMSOL simulations with fixed constraints. The red curve is obtained by applying the method presented in this article.

Funding. Technische Universität Braunschweig (Open Access Publication Funds); Deutsche Forschungsgemeinschaft (EXC-2123 QuantumFrontiers – 390837967).

Disclosures. The author declares no conflicts of interest.

Data availability. Data underlying the results presented in this paper are not publicly available at this time but may be obtained from the authors upon reasonable request.

References

1. G. M. Harry and L. S. Collaboration, "Advanced ligo: the next generation of gravitational wave detectors," Classical Quantum Gravity **27**(8), 084006 (2010).
2. T. Kessler, C. Hagemann, C. Grebing, T. Legero, U. Sterr, F. Riehle, M. Martin, L. Chen, and J. Ye, "A sub-40-mhz-linewidth laser based on a silicon single-crystal optical cavity," Nat. Photonics **6**(10), 687–692 (2012).
3. N. Hinkley, J. A. Sherman, N. B. Phillips, M. Schioppo, N. D. Lemke, K. Beloy, M. Pizzocaro, C. W. Oates, and A. D. Ludlow, "An atomic clock with 10–18 instability," Science **341**(6151), 1215–1218 (2013).
4. T. E. Mehlstäubler, G. Grosche, C. Lisdat, P. O. Schmidt, and H. Denker, "Atomic clocks for geodesy," Rep. Prog. Phys. **81**(6), 064401 (2018).
5. A. Derevianko and M. Pospelov, "Hunting for topological dark matter with atomic clocks," Nat. Phys. **10**(12), 933–936 (2014).
6. E. Savalle, A. Hees, F. Frank, E. Cantin, P.-E. Pottie, B. M. Roberts, L. Cros, B. T. McAllister, and P. Wolf, "Searching for dark matter with an optical cavity and an unequal-delay interferometer," Phys. Rev. Lett. **126**(5), 051301 (2021).
7. Y. Levin, "Internal thermal noise in the ligo test masses: A direct approach," Phys. Rev. D **57**(2), 659–663 (1998).
8. M. Tugolukov, Y. Levin, and S. Vyatchanin, "Thermal noise computation in gravitational wave interferometers from first principles," Phys. Lett. A **382**(33), 2181–2185 (2017).

Optics EXPRESS

9. M. Granata, E. Saracco, N. Morgado, A. Cajgfinger, G. Cagnoli, J. Degallaix, V. Dolique, D. Forest, J. Franc, C. Michel, L. Pinard, and R. Flaminio, "Mechanical loss in state-of-the-art amorphous optical coatings," Phys. Rev. D **93**(1), 012007 (2016).
10. R. Kubo, "The fluctuation-dissipation theorem," Rep. Prog. Phys. **29**(1), 255–284 (1966).
11. Note: In practice, the convergence is fast, as the speed of sound in solids is large compared with the mechanical read-out frequency.
12. COMSOL multiphysics, https://www.comsol.com/. Accessed: 2021-09-18.
13. F. Bondu, P. Hello, and J.-Y. Vinet, "Thermal noise in mirrors of interferometric gravitational wave antennas," Phys. Lett. A **246**(3-4), 227–236 (1998).
14. Y. T. Liu and K. S. Thorne, "Thermoelastic noise and homogeneous thermal noise in finite sized gravitational-wave test masses," Phys. Rev. D **62**(12), 122002 (2000).
15. N. Ismail, C. C. Kores, D. Geskus, and M. Pollnau, "Fabry-pérot resonator: spectral line shapes, generic and related airy distributions, linewidths, finesses, and performance at low or frequency-dependent reflectivity," Opt. Express **24**(15), 16366–16389 (2016).